



# Strategy for double-side friction stir welding of thick Mg4Y3Gd alloy joints

Nadeem Fayaz Lone<sup>1</sup> · Nabeel Ali<sup>1</sup> · Mustufa Haider Abidi<sup>4</sup> · Dhruv Bajaj<sup>1,3</sup> · Touseef Khan<sup>1</sup> · Daolun Chen<sup>3</sup> · Abdulrahman Al-Ahmari<sup>2</sup> · Arshad Noor Siddiquee<sup>1</sup>

Received: 16 March 2023 / Accepted: 24 February 2024 / Published online: 4 March 2024  
© The Author(s), under exclusive licence to Springer-Verlag London Ltd., part of Springer Nature 2024

## Abstract

Defect-free welding of thick sections of Mg alloys is a challenging task, often attempted via double-side friction stir welding (DS-FSW) which generally utilizes a pin length equivalent to ~50% or ~100% of plate-thickness. Nevertheless, tunneling defects often persist in the welded Mg alloys, arising the need to explore intermediate pin-lengths. Thus, in this study, a pin length equivalent to 75% plate-thickness was employed and compared with its 50% and 100% variants, to weld 11.5-mm-thick Mg4Y3Gd alloy plates. The material flow, microstructural, mechanical, and electrochemical aspects were scrutinized with respect to the alteration in pin-length. The evolution of secondary phase particles (SPPs) was also analyzed in different regions of the welded structure. Defect-free welds with ultra-fine grains having a joint efficiency of 97% were obtained using 75% pin length. The segregation of SPPs was observed at the grain boundaries. The microstructure of the fabricated weldments was correlated with the microhardness and tensile analysis. Fractographic examination was performed using SEM, which revealed a fracture type similar to quasi-cleavage. The electrochemical characteristics were assessed through potentiodynamic testing, which demonstrated a substantial enhancement in the anti-corrosion rate of the welded joint due to grain-refinement of the base alloy and dissolution of the yttrium- and gadolinium-rich SPPs.

**Keywords** Double-side friction stir welding · Thick magnesium alloys · Pin design · Tunnel defects

## 1 Introduction

Automotive and aerospace sectors are at the forefront for CO<sub>2</sub> emissions. According to reports, around  $10.7 \times 10^{12}$  kg of CO<sub>2</sub> gas released into the atmosphere annually during 2007 to 2016, of which, around 87% was from the burning of fossil fuel alone [1]. One of the most immediate solutions to alleviate this concern is weight reduction in

transportation vehicles without sacrificing the safety [2]. Magnesium and aluminum alloys are promising solutions for weight reduction and decreasing emissions in a manner which is cost-effective. In comparison to aluminum and steel, the density of magnesium is lower by 36% and 78%, respectively. This makes Mg the lightest structural metal and has attracted a lot of interest [3, 4]. Between 1995 and 2007, magnesium production increased by 390% [5]; this upsurge shows the robust demand for magnesium. Its early applications mainly remained with the automobile sector and has accounted for more than 15% of vehicle weight in the last 10 years, which resulted in reduction in the fuel consumption of around 25% between 1990 and 2005 [6, 7]. Reports indicate that reducing vehicle weight by 10% decreases fuel consumption by 7% [5]. Use of magnesium can revolutionize the evolving electric vehicles too. It can have remarkable impact in enhancing the per charge battery mileage, which is currently one of the main bottlenecks. Magnesium's distinctive properties, such as anti-knock resistance, high strength-to-weight ratio, and electromagnetic shielding, make it a promising material

✉ Arshad Noor Siddiquee  
arshadnsiddiquee@gmail.com

<sup>1</sup> Department of Mechanical Engineering, Jamia Millia Islamia, New Delhi 110025, India

<sup>2</sup> Department of Industrial Engineering, College of Engineering, King Saud University, P.O. Box-800, 11421 Riyadh, Saudi Arabia

<sup>3</sup> Department of Mechanical and Industrial Engineering, Toronto Metropolitan University (Formerly Ryerson University), Toronto, ON M5B 2K3, Canada

<sup>4</sup> Advanced Manufacturing Institute, King Saud University, P.O. Box-800, 11421 Riyadh, Saudi Arabia

for defense and marine applications as well. Because of its neutron absorption capacity and resistance to carbon, it is also used in equipment development in nuclear power plants [8].

Potential applications of magnesium alloys in automobile sector include steering wheel frame, wheel rims, transmission case, and gear control housing [9, 10]. The application of Mg in aviation industry includes thrust reverses, fan frames, and transmission casing [11]. Such applications require joints with high thickness, and fast-emerging applications call for very high thicknesses. To realize the aforementioned potential applications, the attraction for welding thick magnesium plates is increasing.

To take account of the rapid expansion of application of magnesium alloys, the joining of thick magnesium plates via different welding techniques needs to be addressed [12]. Friction stir welding (FSW) has proven to be more efficient than the conventional welding processes [12–17] due to its advantages like low distortion, low residual stress, absence of solidification related defects, no solidification cracking, free from consumable usage, and low energy requirements. The techniques such as laser beam welding (LBW) are employed in joining up to 8–10-mm-thick magnesium plates [18]. Intense heat used in LBW deteriorates the micro-structural morphology of Mg alloys. Hence, the welding of thick Mg sections via FSW proves to be a better proposition.

Notably, most of the published work on Mg-FSW reports joining of thin sections and has generally adopted single-sided FSW. FSW of Mg alloys for thickness greater than 10 mm is rarely reported. This is generally due to the challenges including requirement of a very large shoulder diameter of tool, steep thermal gradient along the thickness, and susceptibility to tool pin failure [13, 19]. Welding of thick plates involves designing tools with a long pin. Consequently, the typical shoulder-diameter to pin-length ratio of 3, which is conventionally required in FSW, necessitates a very large diameter shoulder. Large shoulder diameter increases temperature excessively near the shoulder and is responsible for a very steep thermal gradient along the thickness. In response, two alternatives include the double-sided FSW (DS-FSW) and FSW with a bobbin tool. The DS-FSW is done by welding with a smaller pin length than the weld thickness and then flipping the side of the plate after welding on one side is complete, whereas bobbin tool FSW is performed using a double shoulder tool [20]. Notably, in comparison to bobbin tool FSW, the DS-FSW incurs slightly extra time during flipping the plates; however, bobbin tool FSW can only weld open-ended joints and put huge challenge on the design and material of pin and in managing thickness variation in the plates [21]. Also, while similar apparatus as conventional FSW can be employed for DS-FSW, the tool and control system design complexity increase

in case of bobbin tool FSW [22]. The bobbin tool-pin also experiences multi-axial bending and tension upon entering, increasing its susceptibility to failure. Furthermore, treatment of entry-defect is another challenge encountered upon bobbin tool FSW [22]. Understandably, the bobbin tool also encapsulates the weld zone, allowing limited access for inspection, which is not the case for DS-FSW. Thus, DS-FSW was preferred over bobbin tool in the current study. Nevertheless, literature suggests that double-side welded plates are superior in strength than those welded by conventional single sided FSW [23].

Notably, up to 250-mm-thick sections of lightweight metals are employed in the aerospace sector [24, 25]. For thick sections, the conventional criterion of 3:1 ratio for shoulder-diameter to plate-thickness is neither feasible nor practical. Very large tool shoulders are bound to enormously increase the axial force, spindle torque, and traverse force. Moreover, extremely large shoulder-affected-stir-zones result in low weld integrity too. Importantly, the prime reason for increasing shoulder diameter with plate thickness is to supply additional heat to the high flow stress region at the bottom of plate. However, instead of increasing shoulder diameter and applying single side FSW, decreasing pin length and employing DS-FSW provide a better solution to the above problems. Nevertheless, the pin length variation for DS-FSW has only been explored for 4-mm-thick AA6061 alloy to date [20], resulting in promising outcomes.

This maiden work on 11.5-mm-thick Mg4Y3Gd magnesium alloys presents in-depth analyses on defect formation, microstructural, mechanical characterization, and corrosion behavior. Importantly, a strategy to vary pin-length by keeping shoulder-diameter constant for DS-FSW of 11.5-mm-thick Mg4Y3Gd plates has been analyzed with a view to suggest feasible pin length to shoulder diameter correlation for double sided welding of thick Mg-alloy plates.

## 2 Materials and methods

As-cast Mg4Y3Gd alloy plates having dimensions of 200 mm × 110 mm × 11.5 mm were used as the base alloy. Table 1 depicts the as-received base alloy's major alloying element composition and mechanical properties. The

**Table 1** Mechanical properties and composition of major alloying elements of Mg4Y3Gd

Mechanical properties	Tensile strength (MPa)	Elongation (%)	Micro-hardness (HV)
	163.5	30.56	60
Element (wt%)	Mg	Y	Gd
	Balance	4%	3%

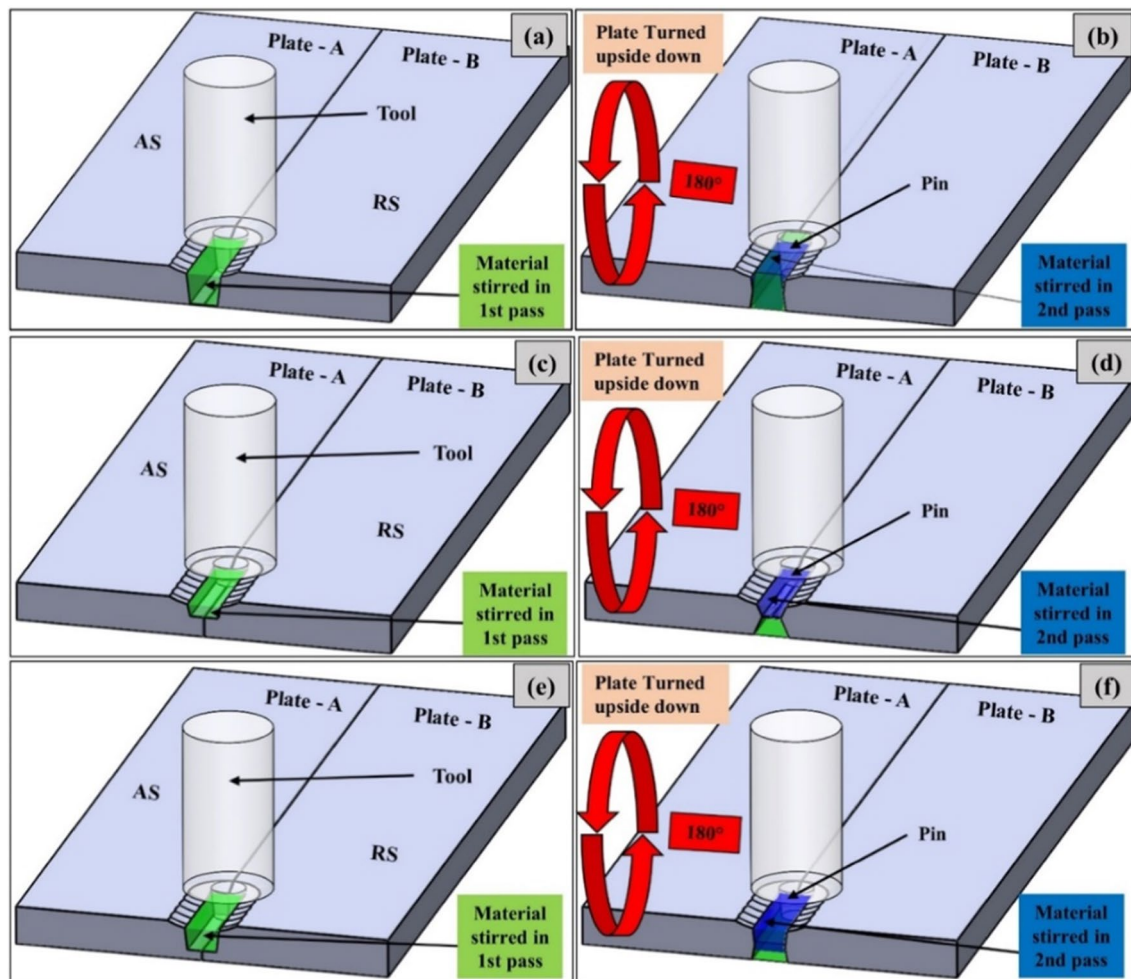


**Fig. 1** Schematic representing FSW setup utilized for Exp. **a, b** No. 1, **c, d** No. 2, and **e, f** No. 3

plates were welded in butt configuration, and the DS-FSW was performed. The plates were flipped upside down after performing FSW on one side, as shown in Fig. 1. Thus, the advancing side (AS) and the retreating side (RS) remained same in both the passes. A HSS tool with a tapered cylindrical cam tri-flute profile and a left-hand thread of approximately 1-mm pitch was used for experimentation, as depicted in Fig. 2. The shoulder diameter and tool tilt angle were maintained at 26 mm and  $2^\circ$ , respectively. A rotational and traverse speed of 710 rpm and 100 mm/min respectively was used to carry out the FSW. Three experiments were carried out by varying the pin length, as depicted in Table 2.

The samples for microstructural examination and tensile testing were wire-cut along the transverse direction of weldments, by employing a computer interfaced wire-electric discharge machine (WEDM). The location of wire-cut tensile and corrosion specimens within the welded plates are shown in Fig. 3a, and the corresponding dimensions are illustrated by Fig. 3b, c. Tensometer of

20 kN capacity was used to conduct the tensile tests. Fractured surface of tensile test specimens were scrutinized under scanning electron microscopy (SEM). The specimens were prepared for microscopic examination using the standard metallographic technique. After grinding and polishing, the samples were etched with Picral solution for 40 s. For the analysis of defects, grain size, and morphology, light microscopy (LM) was utilized. The distribution and chemical composition of secondary phase particles (SPPs) was analyzed by employing a scanning electron microscope coupled with electron dispersive spectroscopy (SEM-EDS). Line intercept technique using ImageJ software was used to measure the grain size. Micro-hardness distribution of the weldments was obtained using Vickers micro-hardness tester. Each indentation was taken at a distance of 0.5 mm at a load of 1 N for a dwell period of 15 s. The corrosion tests for base alloy and welded specimen were conducted using an open circuit potential (OCP) in a three-electrode cell (200 mL) having calomel and platinum as reference and counter electrode, respectively. The

**Fig. 2** Schematic of tools used in **a** Exp. No. 1, **b** Exp. No. 2, and **c** Exp. No. 3

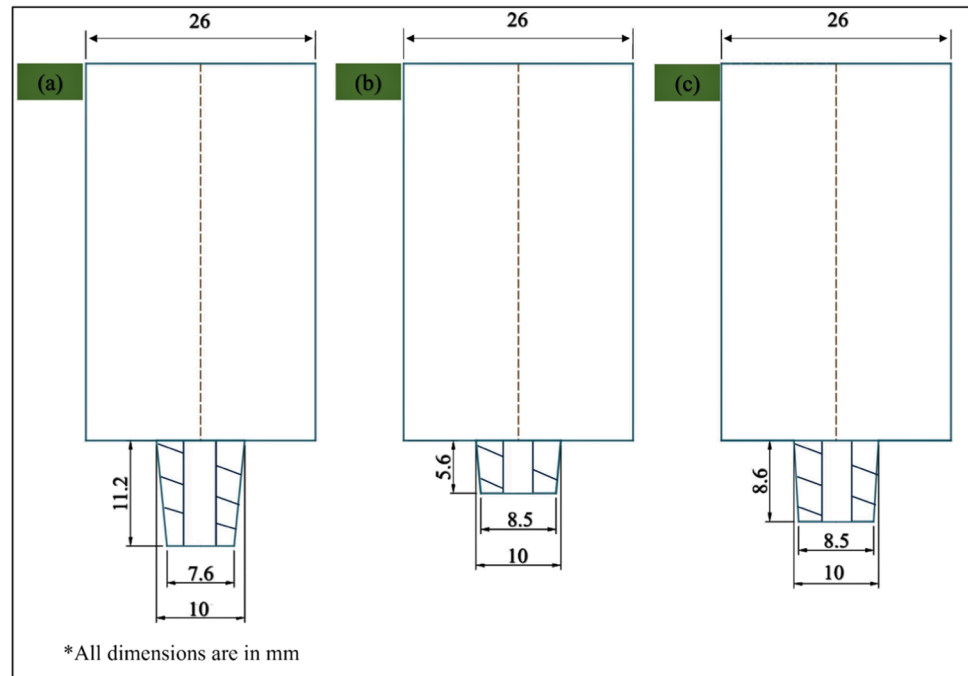


**Table 2** Tool dimensions utilized in DS-FSW

Exp. No	Length (mm)	Tip diameter (mm)	Root dia (mm)
1	11.2	7.6	10
2	5.6	8.5	10
3	8.6	8.5	10

samples were exposed to an aqueous solution of 3.5 M NaCl.

### 3 Results and discussion

#### 3.1 Defect formation analysis using optical macrographs

The transverse sections of welded macrostructures of Exp. Nos. 1–3 are shown in Fig. 4. Top and bottom sides in each macrograph depict the second and first FSW passes, respectively. Each of the welded specimens clearly indicates Shoulder Affected Stir Zone (SASZ), Pin Affected Stir Zone (PASZ), and Thermo-Mechanically Affected Zone (TMAZ). The TMAZ is further categorized into A, B, and C to demarcate changes in morphology with decreasing induced strain in the order of  $C < B < A$ . The interface between SASZ and PASZ is termed as Transition Stir Zone (TSZ). Exp. Nos. 1 and 2 exhibit tunnel defects,

while the Exp. No. 3 produced a defect-free weldment, as observable in Fig. 4.

In Exp. No. 1, which is welded by employing full length of the tool pin (i.e., 11.2 mm), tunnel defect is observed in the TSZ on the AS. During FSW of thick plates, material near the SASZ is significantly hotter than in the PASZ, causing a steep flow stress gradient between the two zones. During welding on one side, the material in the SZ experiences significant strengthening and refinement as a result of severe plastic deformation (SPD) and dynamic recrystallization (DRX). When reverse side welding pass is performed, the base alloy near the shoulder is softened. However, the previously strengthened material increases the flow stress variation, which is manifested in the appearance of TSZ. Thus, the thermal synergy is difficult to maintain across the weld depth, resulting in a defect at the AS-TSZ.

The material ahead of tool is transported to  $180^\circ$  behind it, through the RS, to get consolidated on trailing side. Thus, the material in AS has to travel a larger distance, as compared to the material in RS. Consequently, the material deficiency generally occurs in the AS. In case of single-pass FSW, the material at the bottom of SZ is farthest from the major heat source, i.e., tool shoulder. The material at the shoulder interface is softer, consequently easy to move, and is transported by direct shoulder action. But, for the bottom region, the material is difficult to move, has higher flow stress, and is transported by pin and the induced action. The material movement in the bottom region is therefore difficult and inefficient. Majority of researchers report the tunnel defect at the bottom in AS of the weldments [26–28].



The Exp. No. 2 was carried out using pin length equal to half the plate thickness (i.e., 5.6 mm). A tunnel defect is observed at the bottom in AS after the second pass (i.e., on the reverse side) of the weld, i.e., in SZ-2. Notably, before the reverse pass (on the reverse side), the material in the vicinity of bottom of SZ-1 is strengthened due to pin stirring and induced stresses during first pass. This increases the flow stress at the bottom of SZ-2, leading to a material deficiency at this location. Further, in vertical direction, the left-hand thread supports extrusion of material upward from PASZ to SASZ, increasing the vulnerability of the region to tunneling defects.

The tool geometry was designed with a small shoulder diameter (i.e., shoulder diameter to plate thickness = 2.26) with a view to minimize thermal gradient. The steep thermal gradient also results in large gradient in the flow stress of the SZ material along thickness. The large flow stress gradient causes material flow difficult during first and reverse pass with full pin-length tool as in both passes, the pin encounters deficient material flow leading to tunnel defect. In case of 50% pin-length, the material present mid thickness is poorly stirred which also results in defect.

In Exp. No. 3, the macrostructure clearly demarcates the double stirred zone (DSZ). The weld structure shows uniformity in material flow across DSZ. In comparison to Exp. No. 2, the location of the defect-prone area, i.e., bottom of SZ of the first pass, in this case is closer to the shoulder due to deeper basin of SASZ, which leads to uniform flow stress and improved consolidation. whereas, in comparison to Exp. No. 1, smaller pin length and pin affected region improve the

flow stress consistency between SASZ and PASZ, obviating chances for forming of tunnel at the interface.

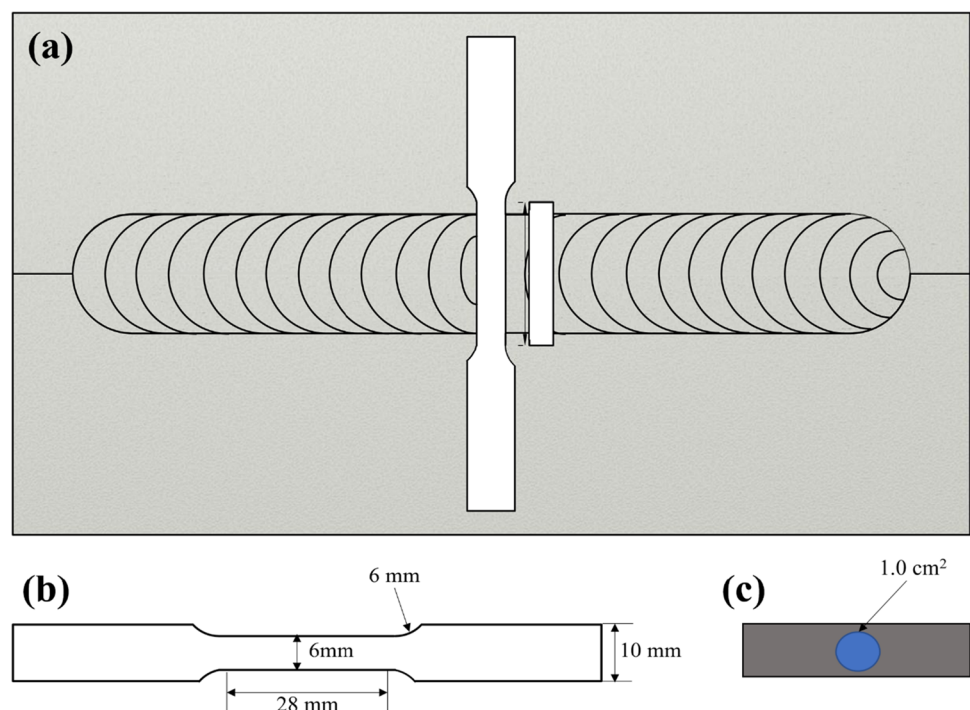
In general, the macrographs of Exp. Nos. 1–3 show more coarsening of grains on the AS compared to the RS. Additionally, the grains in TMAZ of Exp. Nos. 2 and 3 also depict more coarsening in comparison to the Exp. No. 1, indicating a decrease in induced strains in the TMAZ as the pin length decreases.

### 3.2 Analysis of grain morphology using light micrographs

The FSW tool primarily performs two functions: (a) supplying frictional heat input and (b) transport and stirring of the softened material. These two functions are controlled by the process parameters and are the most influential factors in the evolution of microstructure and obtaining defect-free welds. The metallographic examination of each specimen showed grain refinement in all the zones, including Heat Affected Zone (HAZ). The grain refinement in each zone is dependent on the plastic deformation, prevailing temperature, and the strain rate on both sides of the joint line. The effect and dominance of the aforementioned parameters decrease on moving away from the abutting faces.

The micrographs corresponding to the base alloy and tunnel defects of Exp. No. 1 and 2 are shown in Fig. 5. The Exp. Nos. 1 and 2 exhibit a tunneling defect on the AS of the weld, as was previously evident from the macrostructure. The morphology of the defects in Fig. 5b, c indicates layers

**Fig. 3** Schematic illustrations **a** showing the location of tensile and corrosion specimens within the welded plates, **b** tensile specimen dimensions, and **c** an area of 1 cm<sup>2</sup> exposed during corrosion testing



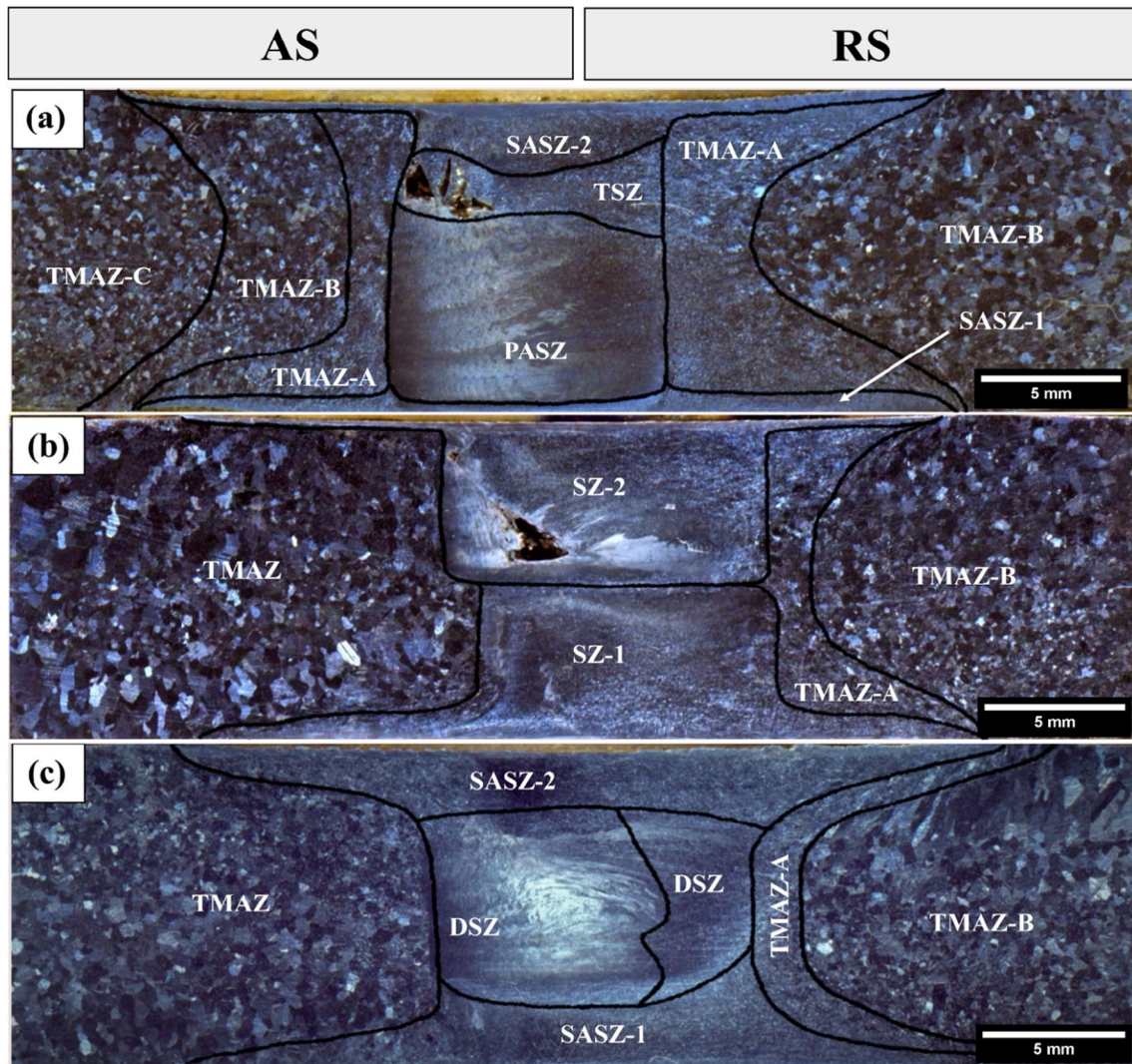


**Fig. 4** Macrographs for **a** Exp. No. 1, **b** Exp. No. 2, and **c** Exp. No. 3

that could not adequately get transported causing inefficient material flow, and this was the core reason behind the defect formation. Essentially, these defects are sensitive to heat input which is controlled by the tool-pin geometry. In the case of thick plates, a gradual thermal gradient is difficult to maintain across the weld depth, thereby causing incoherency in flow stresses resulting in defects.

Further, a close examination of the SZ of defect-free weld, i.e., Exp. No.3, can highlight morphological change along the weld depth. Figure 6 captures the micrographs of SZ corresponding to Exp. No. 3 from top to bottom portions of weld, “top” being the SASZ of the second FSW pass. The corresponding grain size distribution plots are depicted in Fig. 7, which indicates extensive grain refinement and a tendency towards bimodal distribution. According to the existing literature, the presence of rare earth (RE) elements in Mg alloys may reduce the

intensity of DRX in some regions due to their inclination to accumulate at the grain boundaries, thereby augmenting the solute drag effect (SDE) [29]. This can promote grain bimodality. The extensive stirring during FSW can often create heterogeneously strained stir zone, which consists of domains having extremely fine grains due to higher shear strain than the relatively larger yet equiaxed grains due to less severe plastic deformation. Such heterogeneous straining during the stick–slip material movement and shearing also promotes bimodality in the welded structure [30]. During FSW, Low-Angle Grain Boundaries (LAGBs) are formed because of continuous stirring at high temperature. The High-Angle Grain Boundaries (HAGBs) are later formed upon absorbing sufficient dislocations, thereby refining the grains. However, LAGBs cannot be transformed into HAGBs in the case of inadequate heat input, which reduces the action of grain refinement [31].



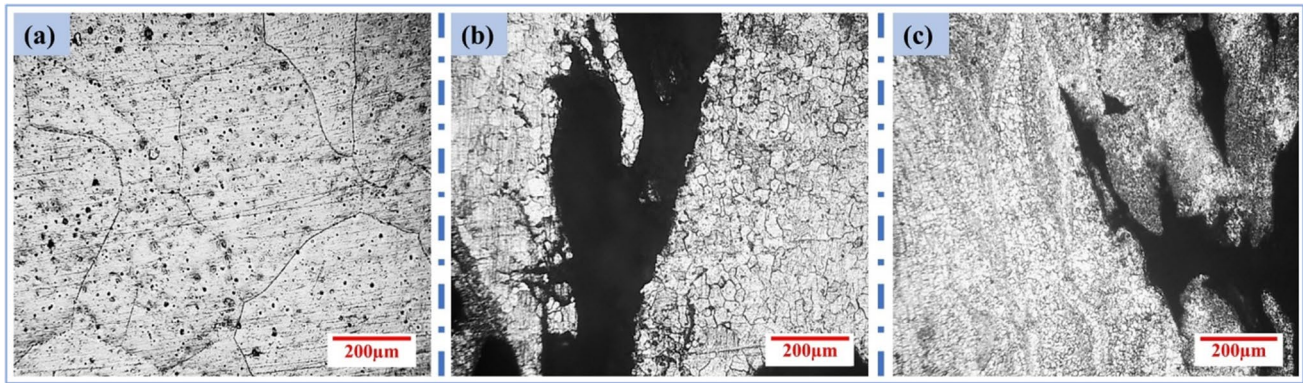


**Fig. 5** Light micrographs for **a** base alloy, **b** Exp. No. 1, and **c** Exp. No. 2

The TMAZs on AS and RS corresponding to Exp. No. 3 are displayed in Fig. 8a and 8b, respectively. The observable disparity in grain size may be ascribed to a wider region which undergoes induced strain on the RS as compared to AS, relative to the center of the tool or the weld line. This is because, on the leading edge of the tool, the incoming material is picked up, gets rotated, and finally, gets deposited behind the tool, as shown in Fig. 8d. Pertinently, the “rotational” aspect of the material transport from the leading to trailing side occurs via the RS and not AS. This greater volume of sheared material leads to a broader expanse of RS-SZ/TMAZ interface region from the joint line or tool center. The analytical aspect of the material flow model described in Fig. 8 has been discussed in detail previously [30]. Thus, even though the strain experienced by the material is greater in the AS, a wide SZ/TMAZ interface manifests into smaller grain size at the RS of the tool as compared to AS (at an identical distance from the joint line). The average grain sizes for TMAZ-AS and TMAZ-RS were measured as 22  $\mu\text{m}$  and 18  $\mu\text{m}$ , respectively. Figure 8c clearly demarcates the presence of smaller grains in the HAZ as compared to the BM. The grain size in HAZ has reduced by around 50% in comparison to base alloy. This reduction in grain size could be attributed to the recrystallization effect on the as-casted structure of the BM [32].

### 3.3 Analysis of chemistry of secondary phase particles using SEM-EDS

The scanning electron (SE) micrographs of Mg base alloy are illustrated by Fig. 9a, b. The base alloy has coarse grain structure with secondary phase particles (SPPs) mainly within the grains (refer to Fig. 9a). The SPPs are highlighted in Fig. 9a by white dashed circles. The micro-segregation of solute particles is also observed as shown in Fig. 9b, which is a common intricacy with casting route [33]. The electron dispersive spectroscopy (EDS) color map and map sum

spectrum of Fig. 9b is shown in Fig. 9b1–b4, c, respectively. The color map reflects segregation of mainly Y/Zr particles.

The SE micrographs of SZ at different locations are illustrated in Fig. 10. A myriad of solute particles is observed in the micrographs. Figure 10b–e show the captured SE micrographs for SASZ-2, DSZ, and SASZ-1, respectively. The micrographs reveal widespread grain refinement in different regions of stir zone; however, very fine grains are observed in the DSZ having an average grain size of 2.52  $\mu\text{m}$ . As observable from Fig. 10b, the segregation of solute particles is chiefly observed at the grain boundaries. The elemental makeup of these SPPs is verified through analysis of the EDS point spectrum (refer to Fig. 10a). The EDS spectrum reveals that yttrium is a significant component of the SPPs. The size of particles found on the grain boundaries is greater than the one found within the grain boundaries (refer to Fig. 10b–e). This behavior suggests the tendency of RE elements to accumulate at the grain boundaries.

According to existing literature, upon plasticization, the RE elements (Y/Gd/Zr) have a notable inclination to accumulate on the grain boundaries [29, 34]. The SZ is directly stirred by the tool pin, leading to substantial plastic deformation in this area. The presence of RE elements at the grain boundaries encourages solute drag or pinning effect, which suppresses dynamic recrystallization [35]. The suppression of DRX results in bimodal grain distribution which is evident from optical micrographs of SZ (Sect. 3.2). However, these secondary phase particles can also lead to decrease in the strength due to localized stress concentration near the grain boundaries, which can become initiation sites for cracks [36]. However, since TMAZ or HAZ are generally the weaker zone, the coarse particles at the grain boundaries in SZ are less likely to cause crack initiations upon monotonic or cyclic loading of the welded joints. Thus, while on one hand, the secondary particles restrain the DRX which allow a bimodal distribution [29] which leads to higher ductility, on the



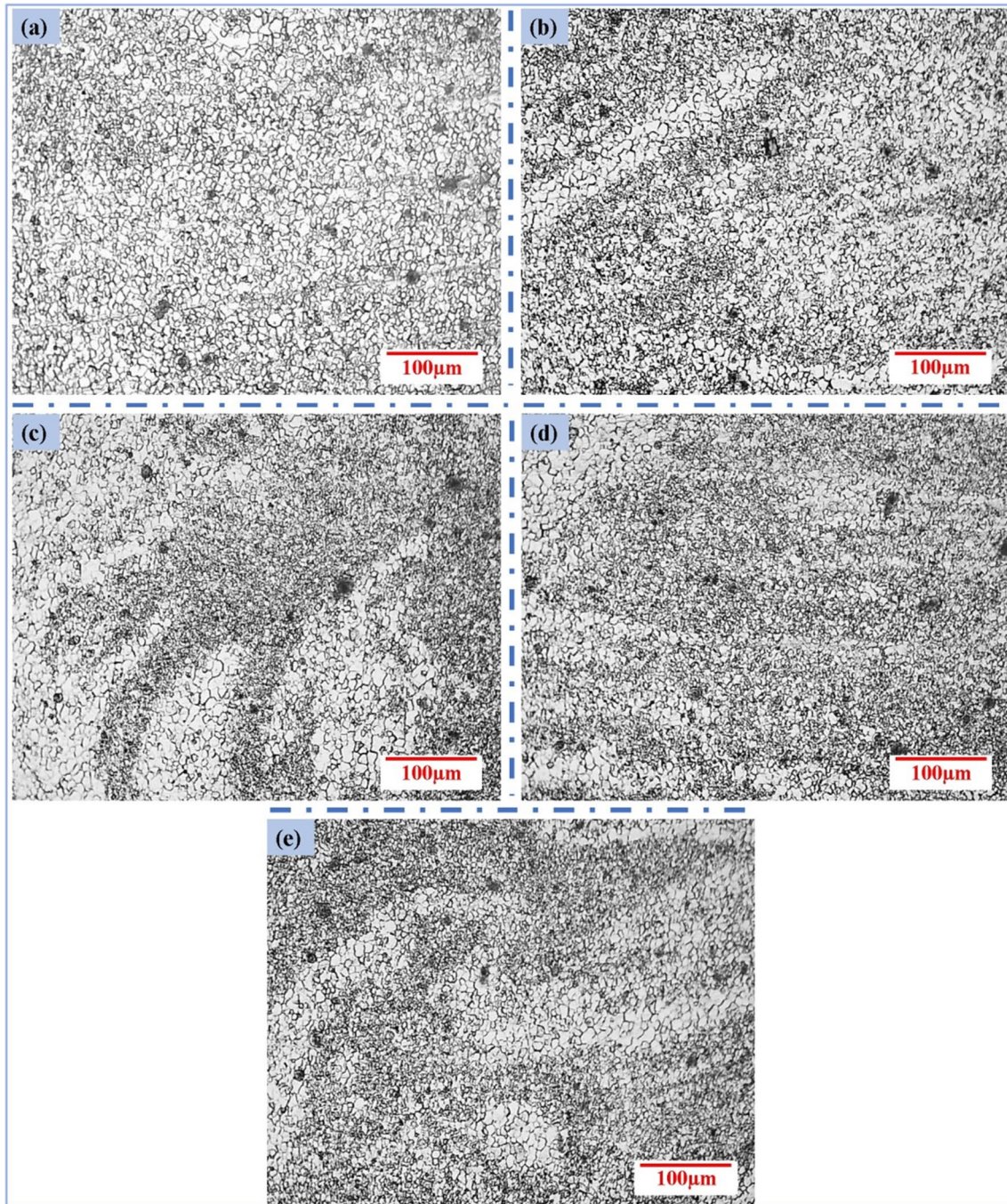


**Fig. 6** Light micrographs corresponding to Exp. No. 3 **a** SASZ-2, **b** interface SASZ-2/DSZ, **c** DSZ, **d** interface SASZ-1/DSZ, and **e** SASZ-1

other hand, the excessive segregation of these particles deteriorates the mechanical integrity of the weld nugget. In addition, the vigorous stirring action and accumulation of Y/Zr/Gd on the grain boundaries cause significant alterations to the strong basal texture of Mg. Moreover, the DS-FSW also results in randomization of the basal texture [37]. The SDE resulted may improve the ductility of the joint [34].

### 3.4 Analysis of microhardness

The micro-hardness distribution over entire transverse section of the defect-free joint from Exp. No. 3 was obtained on a  $0.5\text{ mm} \times 1\text{ mm}$  grid, as illustrated in Fig. 11a. The colored contour map in Fig. 11b demonstrates the obtained results. The contour map was superimposed on the macroscopically distinguished zones (Fig. 4c). The highest micro-hardness



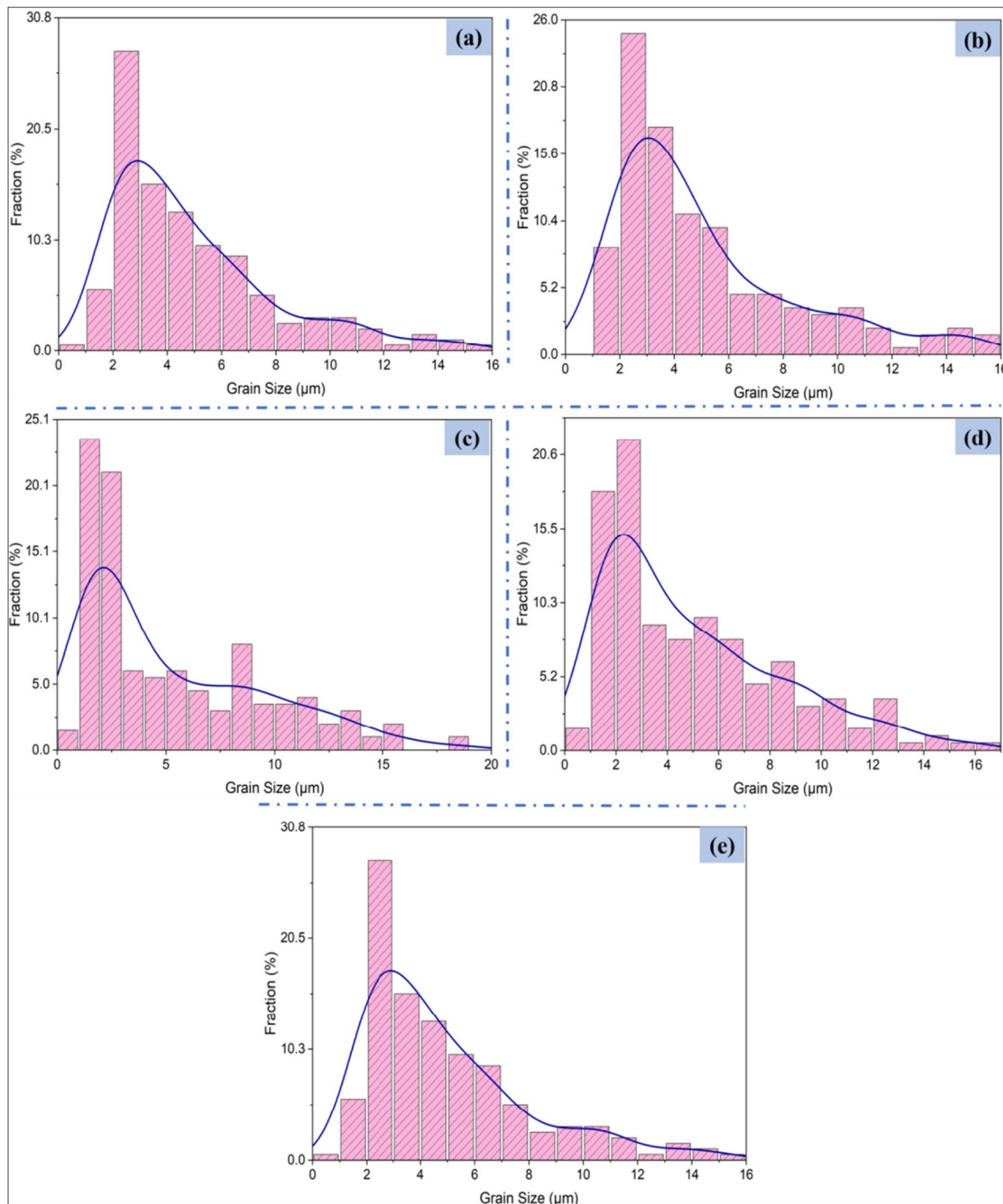


**Fig. 7** Distribution of grain size for Exp. No. 3 **a** SASZ-2, **b** interface SASZ-2/DSZ, **c** DSZ, **d** interface SASZ-1/DSZ, and **e** SASZ-1

of 84.5 HV was measured in the DSZ, which decreased to a value of 50.8 HV in the HAZ on the AS. The average microhardness in the TMAZ on the RS was measured as 70 HV and 65 HV in TMAZ-A and TMAZ-B, respectively, which corroborates with the higher induced strain and subsequent refinement in the TMAZ-A in comparison to TMAZ-B. An average microhardness of 62 HV was measured in

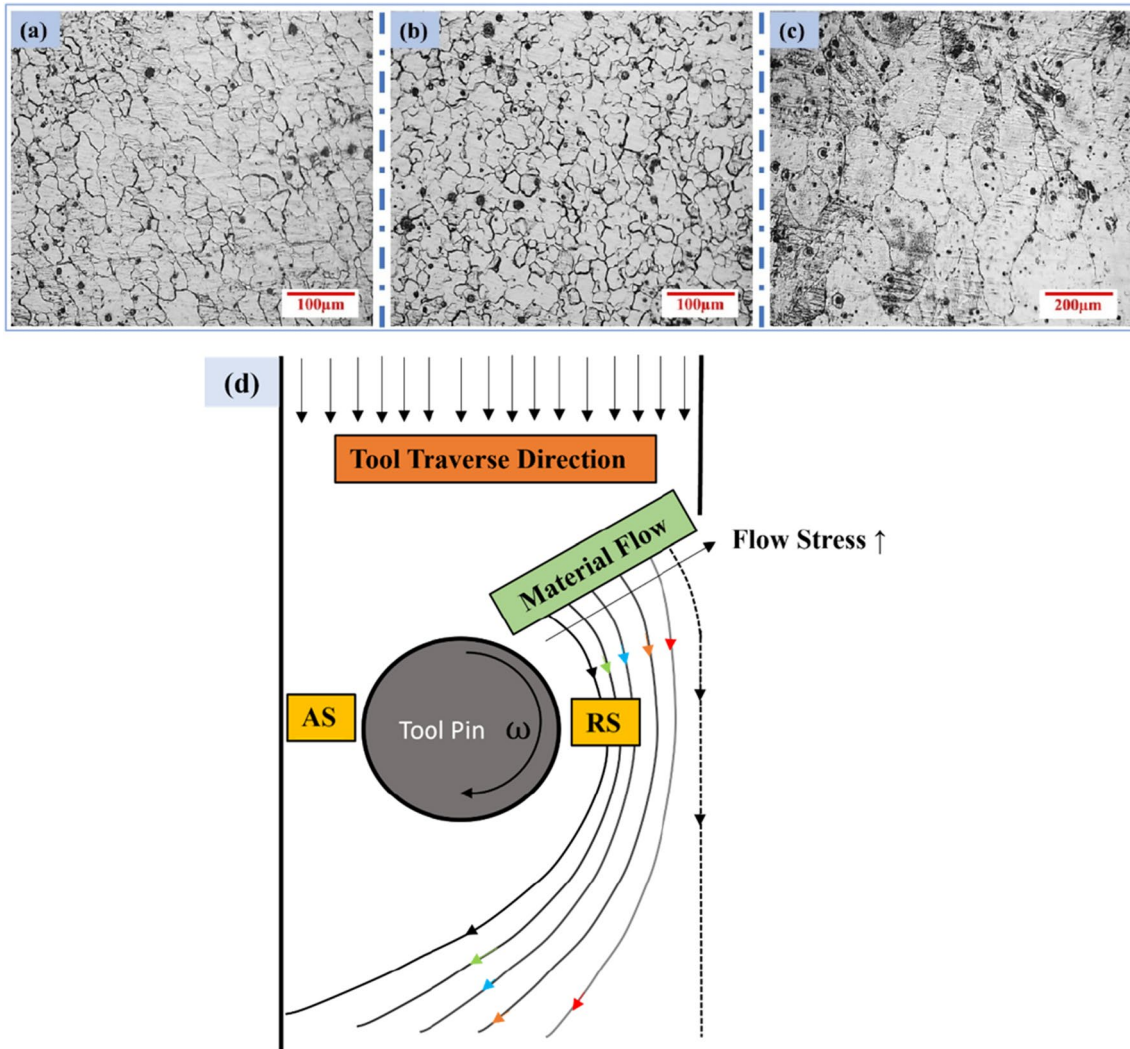
TMAZ on the AS. As explicated above via Fig. 8, the wider TMAZ due to material movement through RS, the average microhardness of TMAZ-RS was observed to be greater than TMAZ-AS. Further, the average value of microhardness obtained in the SASZ-1 and SASZ-2 was 66.3 HV and 64.1 HV, respectively. The material in SASZ-1 undergoes severe plastic deformation and subsequent DRX during the

first pass and experiences further induced strains during the second FSW pass. This results in minimally higher micro-hardness of SASZ-1 as compared to SASZ-2.

The microhardness obtained in different characteristic zones reflects the Hall–Petch effect of grain size as well. The formation of very fine grains in the DSZ due to severe plastic deformation assisted by the DRX is attributed to high microhardness. The extent of grain refinement decreases from DSZ to outer edge due to the decrement in heat input and plastic deformation. It is interesting to observe a uniformly high micro-hardness in the AS-DSZ, also corroborated by its finer grain size in Fig. 10d. Inside the AS-DSZ, the microhardness further peaks in the central region, indicating greater refinement as the distance of the weld-center from the tool shoulder during both the passes is optimized. Furthermore, it was reported that the shear and direct true strain undergone by the material is significantly greater in

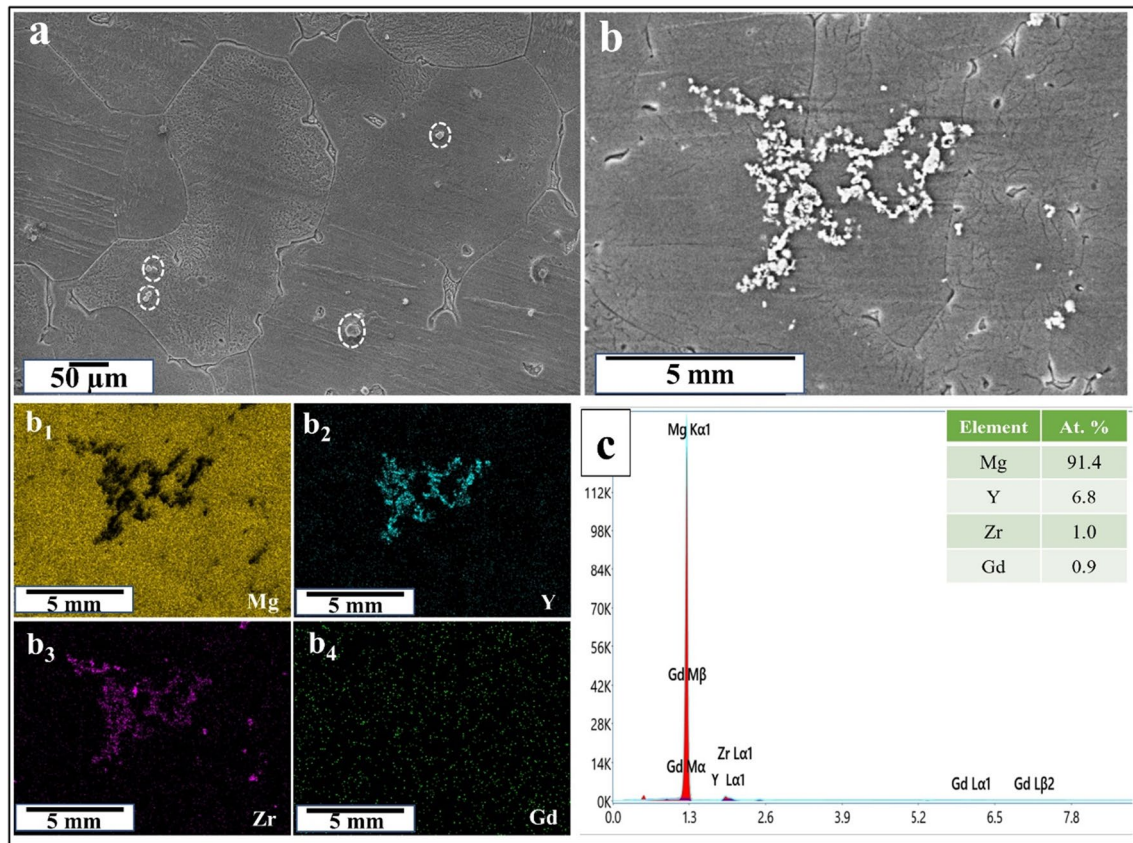
the AS-SZ as compared to RS-SZ [30]. Therefore, AS-DSZ exhibits higher hardness in comparison to RS-DSZ.

Figure 12a–c displays the variation in micro-hardness in the transverse direction at a location of 5 mm below the top surface of the second pass for Exp. Nos. 1–3. All the welds showed the highest microhardness in SZ and a similar decreasing trend from the weld center to the HAZ. These results are in line with the grain size observed in each zone. Further, each weldment showed fluctuation in microhardness values. From the observation of the optical micrographs, the heterogeneity in grain size is evident. This behavior may be attributed to the particle stimulated nucleation (PSN)/pinning effect (PE). The presence of solute particles on the grain boundaries prevents grain growth and enhances the process of DRX, which thereby may result in heterogeneous microstructure [38, 39]. In addition, the left-hand threaded cam tri-flute pin profile



**Fig. 8** a–c Light micrographs for Exp. No. 3 a TMAZ-AS, b TMAZ-RS, and c HAZ. d Depicting increase in induced strains





**Fig. 9** a, b SEM images of base alloy. b<sub>1</sub>–b<sub>4</sub>, c EDS color map and map sum spectrum corresponding to Fig. 8b, respectively

upholds such heterogeneity in grain morphology and consequent fluctuation in micro-hardness.

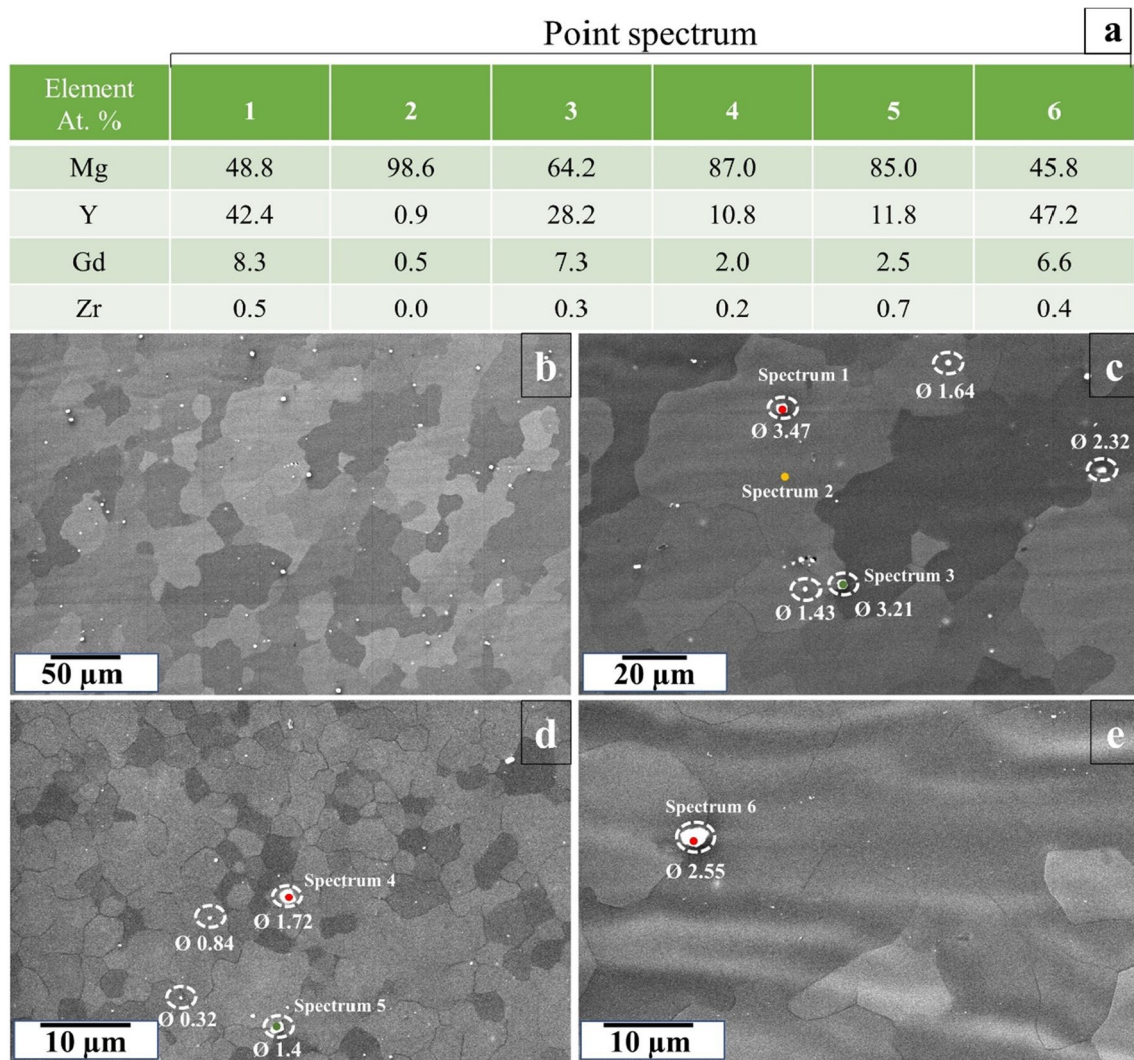
### 3.5 Tensile and fracture mechanism analysis

Figure 13 illustrates the engineering stress–strain graphs for the weldments of Exp. Nos. 1–3 and the base alloy. Table 3 provides information about the tensile properties and fracture location of all the specimens. The base alloy has an ultimate tensile strength ( $\sigma_{UTS}$ ) of 163.5 MPa and a percentage elongation ( $\delta$  %) of 30.56%.

A considerable amount of work on mechanical properties, including tensile strength, is published on magnesium plates having a thickness less than 10 mm. For plate thickness of less than 7 mm, weld efficiencies of 99% [40], 96.7% [16], and ~65% [41] are reported. For the 10-mm-thick AZ31 Mg alloy, similar efficiencies were reported for bobbin tool FSW and conventional FSW [42]. Hejazi et al. [20] carried DS-FSW on 4-mm-thick AA6061-T913 aluminum alloy and obtained joint efficiency ranging from 23.3 up to 49.2%, which indicates that DS-FSW does not necessarily allow high joint efficiencies, and suitable pin length designs are crucial. Mechanical properties of thicker sections of magnesium

alloys are rarely reported. However, in one typical case of 20-mm-thick  $Mg_{95.81}Y_{1.93}Nd_{1.59}Gd_{0.4}Zr_{0.25}Fe_{0.02}$  rolled and subsequently heat-treated plates, the joint efficiency has reached 82.6% via DS-FSW [13], hinting the potential success of this technique, as corroborated here. Also, the bobbin tool FSW of 3-mm-thick AZ31B twin roll cast Mg alloy lately yielded ~68% joint efficiency at room temperature [43]. In the present study, using the optimal pin length in Exp. No. 3, the joint efficiency of 97.2% was attained. A significant percentage elongation of 18.18% was also obtained in this case. A comparative summary of the obtained joint efficiency and UTS with several studies employing DS-FSW, bobbin tool FSW, and conventional FSW is shown in Table 4.

In the literature, the tensile failure location of FS welded samples is generally reported at the TMAZ [45], HAZ [46], or at the AS SZ/TMAZ interface [41] of the weld. The failure may also occur in both the SZ and at the SZ/TMAZ interface [47], depending on double twinning or compression twinning caused due to non-uniform deformation rate or excessive stress. Moreover, Commin et al. [48] reported that the failure location of a joint can also be influenced by the process parameters, and it may occur in the RS of the



**Fig. 10** a EDS point spectrum results. b–e SEM corresponding to Exp. No. 3 b, c SASZ-2, d DSZ, and e SASZ-1

joint. The tensile samples from Exp. Nos. 1 and 2 failed from the SZ of the AS and exhibited low tensile strength due to the presence of tunnel defects. In Exp. No. 3, the sample fractured at the junction of the TMAZ and HAZ. The SZ was strengthened due to grain refinement, whereas the HAZ was weakened. Furthermore, there is a morphology discontinuity at the TMAZ/HAZ junction, making it a stress-concentrated region, which contributed to the failure of the sample.

The UTS and elongation values given in Table 3 are averaged for three samples which had been subjected to uniaxial tensile tests (typically shown in Table 3). Notably, during FSW, the size and shape of the defect can vary along the weld length. This is primarily because of disparity in the thermal cycles experienced by the material at different positions from the location of the initial tool plunge. Hence, the defect morphology was also checked to be chiefly similar

for the three tensile specimens tested for Exp. Nos. 1 and 2, while all the specimen for Exp. No. 3 were found to be defect free.

Figure 14a shows the low-magnification FESEM fractograph corresponding to the defect-free weld obtained in Exp. No. 3. The fractured surface is composed of cleavages and dimples. As Mg has a hexagonal close-packed (HCP) structure, the resolved shear stress of non-basal planes is temperature-dependent. It is reported that the ductile to brittle transition (DBT) in the case of magnesium alloys occurs between the room temperature and 250 °C [34]. This temperature is achievable in FSW. Upon further magnification of Fig. 14a, the ductile (A), transition (B), and brittle (C) regions can be clearly delineated, as shown in Fig. 14b. The ductile region is characterized by shallow and elongated dimples. The brittle region depicts near to complete DBT, as indicated by the red oval



**Fig. 11** **a** Indentation grid across the transverse section of the welded sample for Exp. No. 3. **b** Microhardness contour map corresponding to Exp. No. 3

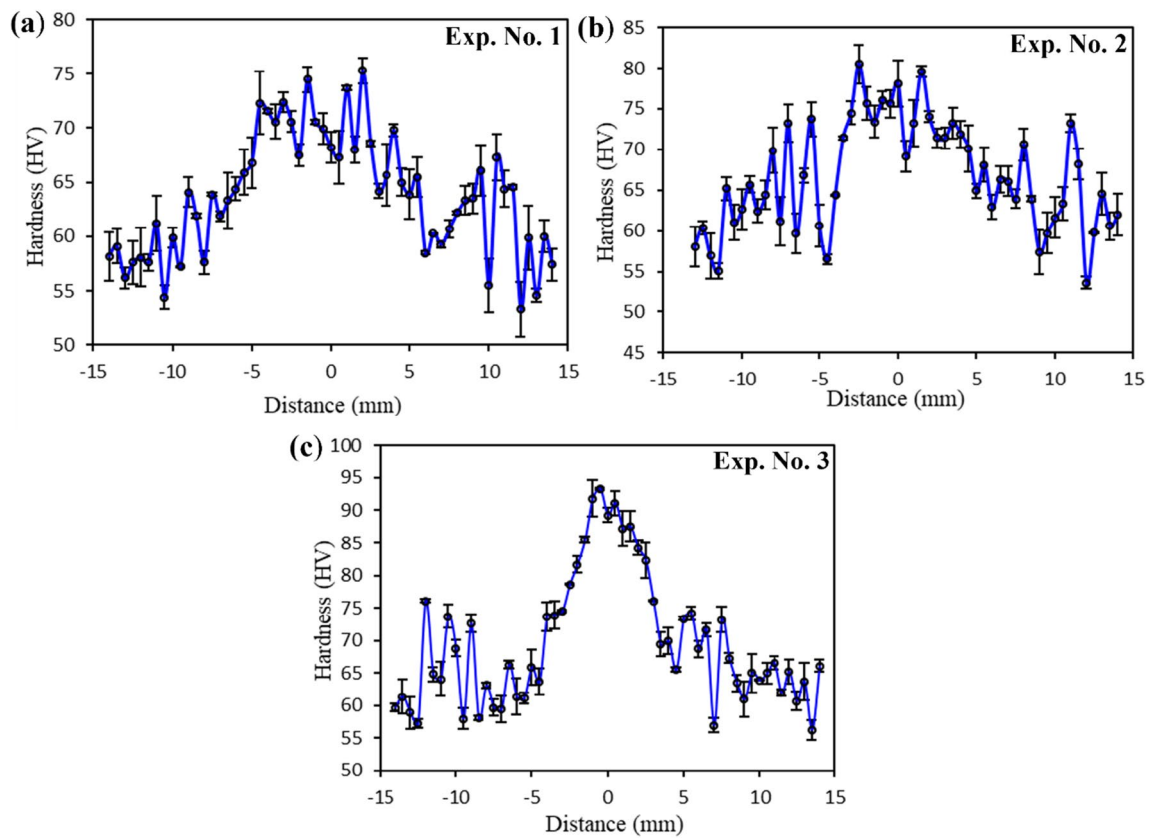
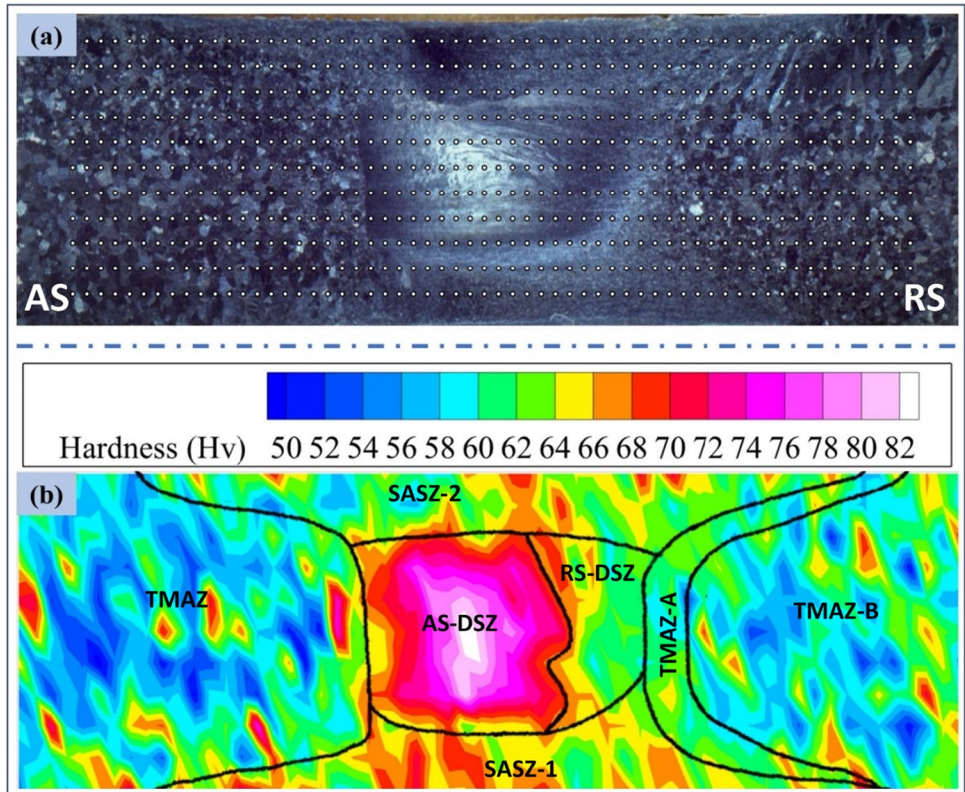


**Fig. 12** **a–c** Micro-hardness variation in transverse direction for Exp. Nos. 1–3

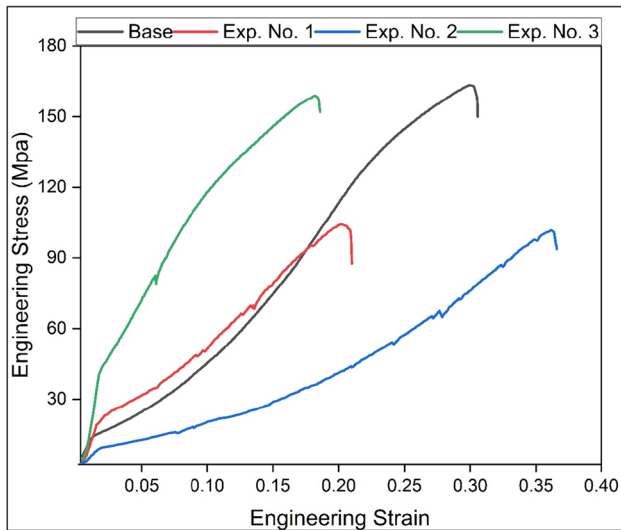


**Fig. 13** Engineering stress–strain plots for welds obtained in Exp. Nos. 1–3 and base alloy

shape in Fig. 14c. Further, Fig. 14d illustrates the intergranular crack (region F in Fig. 14d), which is a brittle failure characteristic produced by decohesion of grains in crystalline materials. Multiple intergranular failure paths can be observed, which creates a river pattern, as indicated by the yellow line in Fig. 14e. Therefore, the decrease in percentage elongation is in agreement with the fractographic analysis.

### 3.6 Electrochemical behavior

Since the application of Mg WE43 alloy in the aerospace industry is gaining momentum, the potential of its anti-corrosion treatment is also enticing attention. The burgeoning of anti-corrosion treatments has increased the acceptability of magnesium in the aerospace and automobile industries. The anti-corrosion treatment methods include fabrication of high purity alloys [49], surface modification with laser annealing

[50], coating of protective films [51], and microstructure refinement [52].

The light micrographs of the base metal and welded specimens corresponding to Exp. No. 3 before and after the corrosion tests are shown in Fig. 15. The BM has coarse grain structure with an average grain size of 240  $\mu\text{m}$ , whereas the SZ of the sample from Exp. No. 3 has fine grains with an average grain size of 12  $\mu\text{m}$ . The fine grains resulted from SPD and DRX. After the electrochemical corrosion test, the microstructure of the BM indicates more severe corrosion as compared to welded joints, which can be observed by comparing Fig. 15c, d. This behavior is chiefly attributed to the larger grain size and a higher density of coarse intermetallic compounds (IMCs) which are present in the RE-Mg alloy BM. During the PDP test, IMCs act as cathodes and subsequently form a galvanic couple with the matrix. During FSW, IMCs either dissolve within the matrix phase at process heat or disintegrate into very fine particles as a result of SPD (refer to Fig. 10). Thus, a weak galvanic couple is formed, and consequently, the corrosion rate is improved in the welded samples of Exp. No. 3.

Further, the potentiodynamic polarization plots for BM and welded specimen are illustrated by Fig. 15e. The corrosion current density ( $I_{\text{corr}}$ ) and reference voltage ( $E_{\text{corr}}$ ) were obtained using the intersection of cathodic and anodic Tafel plots by extrapolating the potentiodynamic polarization plots. The corrosion current density for the welded specimen is 7.14 times lower than the base metal. This indicates an improvement in the corrosion resistance of the welded sample. Moreover, a lower negative value of corrosion potential expresses higher corrosion resistance. The obtained corrosion rates in mils penetration per year (mpy) for the welded specimen and the BM are 19.83 and 141.52 mpy, respectively. In the Tafel plots, the anodic curve of the BM has a slightly steeper slope compared to the welded sample. A steeper anodic slope indicates a faster anodic reaction rate, implying higher production of anions or a faster dissolution of metal. The results from PDP tests also show improvement in corrosion rate after

**Table 3** Tensile properties corresponding to welds obtained through Exp. Nos. 1–3

Exp. No.	UTS (MPa)	% Elongation	Fracture Location	Image
1	104.3	20.23	SZ-AS	
2	101.7	36.15	SZ-AS	
3	158.9	18.18	TMAZ/HAZ-RS	



**Table 4** Comparative summary of obtained mechanical properties and corresponding plate thickness for FSW of Mg alloys

Ref	Mg alloy	Thickness (mm)	Technique	Joint efficiency (%)	UTS (MPa)
Current study	Mg4Y3Gd (as-cast)	11.50	DS-FSW	97.2	158.9
[13]	Mg <sub>95.81</sub> Y <sub>1.93</sub> Nd <sub>1.59</sub> Gd <sub>0.4</sub> Zr <sub>0.25</sub> Fe <sub>0.02</sub> (rolled and subsequently heat-treated)	20.00	DS-FSW	82.6	277.6
[36]	AZ31B with 0.5 wt% Ce	5.00	FSW	99	270
[37]	AZ31B (rolled)	6.00	FSW	88.1	208
[38]	AZ31B-H24	4.95	FSW	~65	201
[43]	AZ31B (twin roll cast)	3.00	Bobbin tool FSW	~68	~198
[42]	AZ31	10.00	Bobbin tool FSW	84	214.8
			FSW	85	219.2
[44]	AZ31 to AM60 (dissimilar welding)	5.00	DS-FSW	88.4	247

FSW, thus provide evidence and agree with the optical micrograph images.

The formation of passivation zone is not observed in Fig. 15e. The formation of MgO as a protective layer is observed when the Mg is exposed to air. However, this poor protective surface film is highly soluble in most aqueous environments. Moreover, the protective layer formed in Mg incompletely covers the underlying bulk metal or can be easily penetrated [53]. When Mg is exposed to an aqueous solution of NaCl, the MgO (solid) layer reacts with H<sub>2</sub>O (liquid) to form Mg(OH)<sub>2</sub> (solid) layer. MgO and Mg(OH)<sub>2</sub> films are formed as bottom and cap layers, respectively

[54]. However, both these layers are soluble in acidic and neutral aqueous solutions. Therefore, the quasi-passive layers formed dissolve, thereby exposing the metal to further corrosion. This process hinders the formation of a strong passivation film in Mg-based alloys.

The literature suggests that the smaller grains in the WE43 series enhance the chances of the formation of a protective layer over the surface [55]. Higher grain refinement leads to more grain boundaries, which in turn decreases the formation of the galvanic couple between the grain boundary and the core [56, 57]. Large grains are more prone to corrosion, resulting in faster degradation.

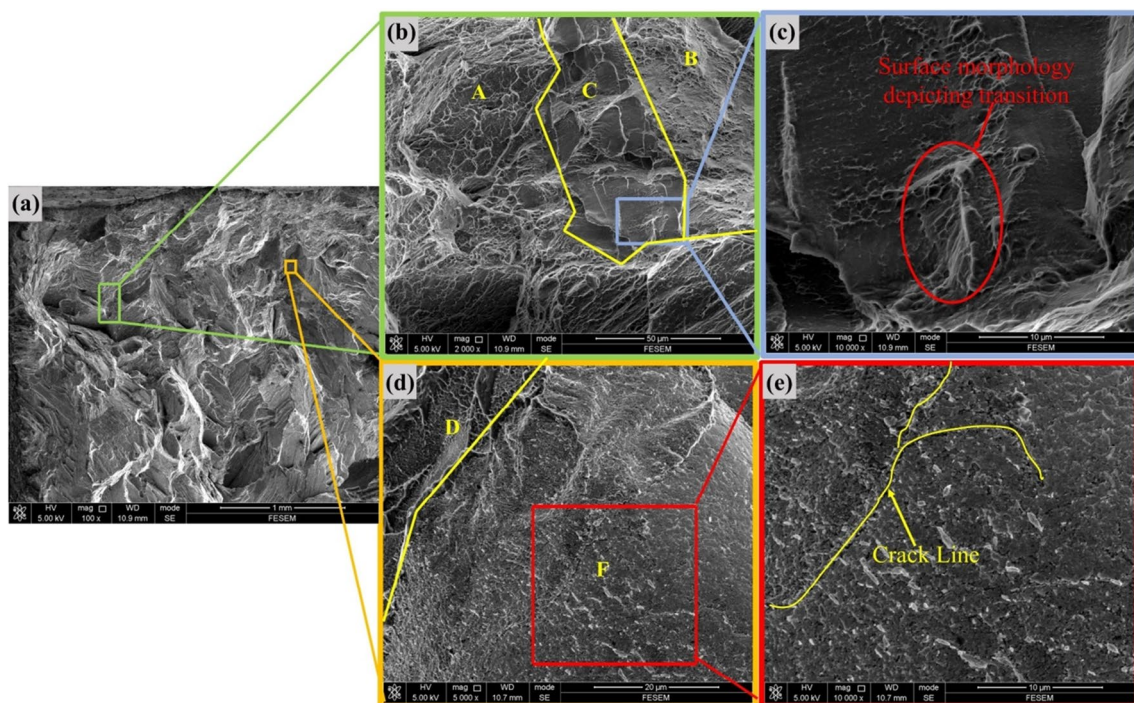
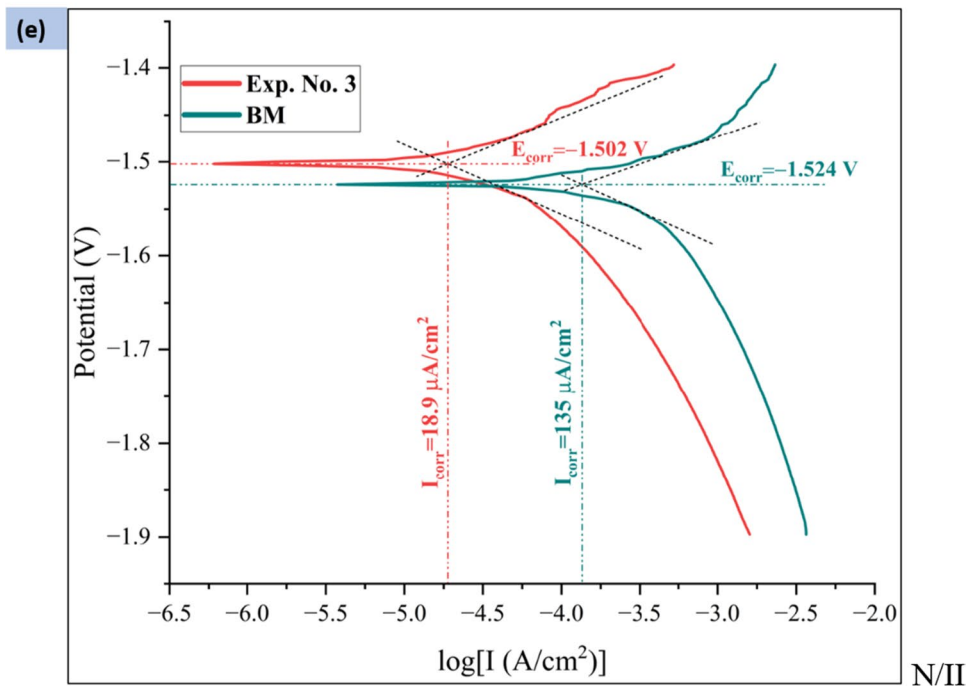
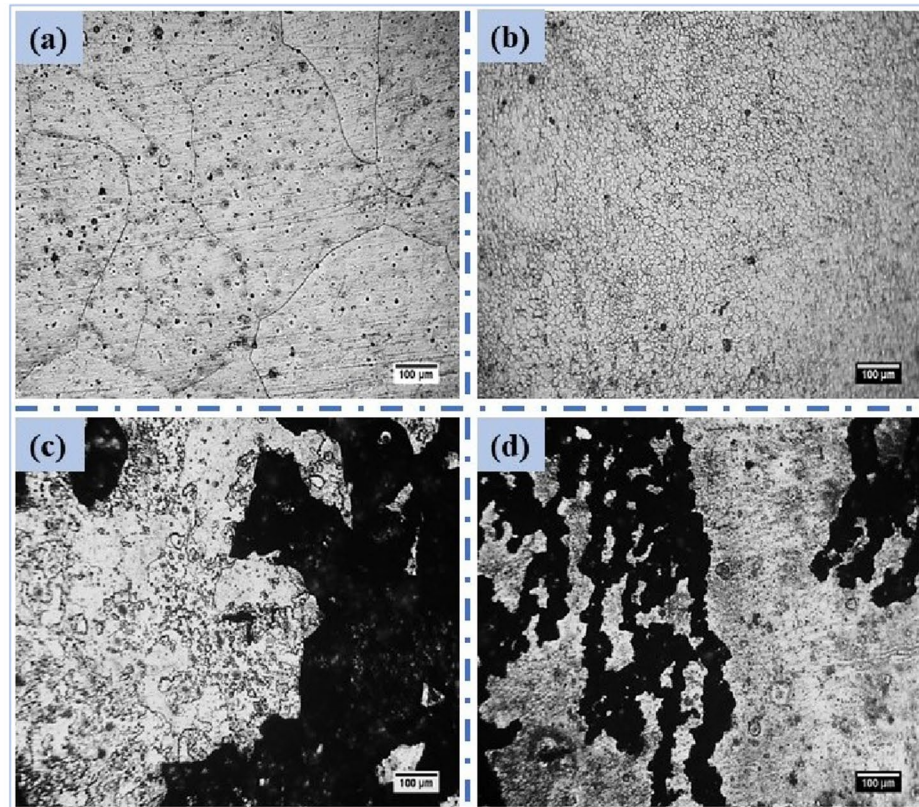


**Fig. 14** FESEM fractographs corresponding to Exp. No. 3. **a** Low-magnification image. **b** High-magnification image depicting A-ductile, B-transition, and C-brittle regions. **c** Transition region B depicting DBT. **d, e** Intergranular crack with river pattern in transition region B

**Fig. 15** **a** Optical microscopy image of BM before corrosion. **b** Optical microscopy image of welded specimen corresponding to Exp. No. 3 before corrosion. **c** Optical microscopy image of BM after corrosion. **d** Optical microscopy image of welded specimen corresponding to Exp. No. 3 after corrosion. **e** Potentiodynamic curves of BM and welded specimen



## 4 Conclusions

In this experimental study, DS-FSW of 11.5-mm-thick Mg3Y4Gd alloy was successfully performed with a pin length of 8.6 mm ( $\frac{3}{4} \times$  platethickness), attaining a high

joint efficiency of 97%. The variation in pin length tremendously affects the mechanistic dynamics and material movement. A relatively smaller pin length of 5.6 mm ( $\frac{1}{2} \times$  platethickness) suffers from defect-prone areas in the SZ bottom, whereas a pin length of 11.2 mm



( $\approx$  platethickness) exhibits significant flow stress incoherency along with the weld depth.

The double stirred region welded with a pin length of 8.6 mm shows a significant disparity in grain size along with the weld depth. Further, a tendency towards bimodal grain size distribution was also observed. The bimodality is also caused due to the accumulation of rare earth elements at the grain boundaries, promoting pinning/solute drag effect, consequently suppressing dynamic recrystallisation. This region exhibits a maximum microhardness of 84.5 HV. The fractographs corresponding to this weld indicated a ductile to brittle transition during FSW. In the transition region, intergranular cracks were observed in a river-like pattern. The extensive grain refinement in the SZ due to severe plastic deformation leads to improvement in the electrochemical behavior of the welded specimen. A large number of grain boundaries decrease the formation of galvanic couples and enhance the formation of protective layer on the surface, thereby increasing the corrosion resistance.

**Author contribution** All authors contributed equally to this work.

**Funding** The authors are thankful to Researchers Supporting Project number (RSPD2024R1092), King Saud University, Riyadh, Saudi Arabia, for funding this work.

## Declarations

**Consent to participate** All the authors consent to participate in this work.

**Consent for publication** All the authors in this work have consented to publish this manuscript.

**Competing interests** The authors declare no competing interests.

## References

- Masood Chaudry UM, Tekumalla S, Gupta M, Jun TS, Hamad K (2022) Designing highly ductile magnesium alloys: current status and future challenges. *Crit Rev Solid State Mater Sci* 47(2):194–281. <https://doi.org/10.1080/10408436.2021.1947185>
- Zhu Y, Chen G, Zhou Y, Shi Q, Zhou M (2023) Achieving synergistic strength-ductility-corrosion optimization in Mg-Li-Al-Zn alloy via cross-pass friction stir processing. *J Alloy Compd* 959:170581. <https://doi.org/10.1016/j.jallcom.2023.170581>
- Harooni M, Kovacevic R (2017) Laser welding of magnesium alloys: issues and remedies. In: Aliofkhaezrai M (ed) *Magnesium alloys*. IntechOpen
- Yuan S, Xia Q, Long J, Xiao G, Cheng X (2020) Study of the microstructures and mechanical properties of ZK61 magnesium alloy cylindrical parts with inner ribs formed by hot power spinning. *Int J Adv Manuf Technol* 111:851–860
- Shrestha S (2010) Magnesium and surface engineering. *Surf Eng* 26(5):313–316. <https://doi.org/10.1179/026708410X12736782825894>
- Reuters (2012) GM tests magnesium sheet metal to take weight of cars. Chicago turbine. <https://www.chicagotribune.com/news/ct-xpm-2012-10-23-sns-rt-gm-magnesium-pix11e8ln33t-20121023-story.html>. Accessed 17 Nov 2022
- Blawert C, Hort N, Kainer KU (2004) Automotive applications of magnesium and its alloys. *Trans Indian Inst Met* 57(4):397–408
- Froes FH, Eliezer D, Aghion E (1998) The science, technology, and applications of magnesium. *JOM* 50:30–34. <https://doi.org/10.1007/s11837-998-0411-6>
- Aghion E, Bronfin B, Eliezer D (2001) The role of the magnesium industry in protecting the environment. *J Mater Process Technol* 117(3):381–385. [https://doi.org/10.1016/S0924-0136\(01\)00779-8](https://doi.org/10.1016/S0924-0136(01)00779-8)
- Kulekci MK (2008) Magnesium and its alloys applications in automotive industry. *Int J Adv Manuf Technol* 39:851–865. <https://doi.org/10.1007/s00170-007-1279-2>
- Luo AA (2013) Magnesium casting technology for structural applications. *J Magnes Alloys* 1(1):2–22. <https://doi.org/10.1016/j.jma.2013.02.002>
- Pan F, Xu A, Ye J, Tang A, Jiang X, Ran Y, Du W (2017) Effects of rotation rate on microstructure and mechanical properties of friction stir-welded Mg-5Al-1Sn magnesium alloy. *Int J Adv Manuf Technol* 91:389–397
- Weng F, Liu Y, Chew Y, Lee BY, Ng FL, Bi G (2020) Double-side friction stir welding of thick magnesium alloy: microstructure and mechanical properties. *Sci Technol Weld Joining* 25(5):359–368. <https://doi.org/10.1080/13621718.2019.1706810>
- Mishra RS, Ma ZY (2005) Friction stir welding and processing. *Mater Sci Eng R Rep* 50(1–2):1–78. <https://doi.org/10.1016/j.mser.2005.07.001>
- Gangil N, Maheshwari S, Siddiquee AN, Abidi MH, El-Meligy MA, Mohammed JA (2019) Investigation on friction stir welding of hybrid composites fabricated on Al-Zn-Mg-Cu alloy through friction stir processing. *J Market Res* 8(5):3733–3740. <https://doi.org/10.1016/j.jmrt.2019.06.033>
- Padmanaban G, Balasubramanian V (2010) An experimental investigation on friction stir welding of AZ31B magnesium alloy. *Int J Adv Manuf Technol* 49:111–121
- Abdolahzadeh A, Omidvar H, Safarkhanian MA, Bahrami M (2014) Studying microstructure and mechanical properties of SiC-incorporated AZ31 joints fabricated through FSW: the effects of rotational and traveling speeds. *Int J Adv Manuf Technol* 75:1189–1196
- Marya M, Edwards GR (2001) Factors controlling the magnesium weld morphology in deep penetration welding by a CO2 laser. *J Mater Eng Perform* 10:435–443. <https://doi.org/10.1361/105994901770344854>
- Buchibabu V, Reddy GM, De A (2017) Probing torque, traverse force and tool durability in friction stir welding of aluminum alloys. *J Mater Process Technol* 241:86–92. <https://doi.org/10.1016/j.jmatprotec.2016.11.008>
- Hejazi I, Mirsalehi SE (2016) Effect of pin penetration depth on double-sided friction stir welded joints of AA6061-T913 alloy. *Trans Nonferrous Met Soc China* 26(3):676–683. [https://doi.org/10.1016/S1003-6326\(16\)64158-4](https://doi.org/10.1016/S1003-6326(16)64158-4)
- Fuse K, Badheka V (2019) Bobbin tool friction stir welding: a review. *Sci Technol Weld Joining* 24(4):277–304. <https://doi.org/10.1080/13621718.2018.1553655>
- Wang GQ, Zhao YH, Tang YY (2020) Research progress of bobbin tool friction stir welding of aluminum alloys: a review. *Acta Metallurgica Sinica (English Letters)* 33:13–29. <https://doi.org/10.1007/s40195-019-00946-8>
- Kumar AR, Varghese S, Sivapragash M (2012) A comparative study of the mechanical properties of single and double sided friction stir welded aluminium joints. *Proc Eng* 38:3951–3961. <https://doi.org/10.1016/j.proeng.2012.06.452>

24. MacKenzie DS, Forge V (2005) Heat treating aluminum for aerospace applications. *Heat Treating Progress* 5(4):37–43
25. Moideuddin K, Siddiquee AN, Abidi MH, Mian SH, Mohammed MK (2021) Friction stir welding of thick plates of 4y3gd mg alloy: an investigation of microstructure and mechanical properties. *Materials* 14(22):6924. <https://doi.org/10.3390/ma14226924>
26. Mehta KP, Badheka VJ (2016) A review on dissimilar friction stir welding of copper to aluminum: process, properties, and variants. *Mater Manuf Processes* 31(3):233–254. <https://doi.org/10.1080/10426914.2015.1025971>
27. Xue P, Ni DR, Wang D, Xiao BL, Ma ZY (2011) Effect of friction stir welding parameters on the microstructure and mechanical properties of the dissimilar Al–Cu joints. *Mater Sci Eng, A* 528(13–14):4683–4689. <https://doi.org/10.1016/j.msea.2011.02.067>
28. Qian J, Li J, Sun F, Xiong J, Zhang F, Lin X (2013) An analytical model to optimize rotation speed and travel speed of friction stir welding for defect-free joints. *Scripta Mater* 68(3–4):175–178. <https://doi.org/10.1016/j.scriptamat.2012.10.008>
29. Asqardoust S, Hanzaki AZ, Abedi HR, Krajnak T, Minárik P (2017) Enhancing the strength and ductility in accumulative back extruded WE43 magnesium alloy through achieving bimodal grain size distribution and texture weakening. *Mater Sci Eng, A* 698:218–229. <https://doi.org/10.1016/j.msea.2017.04.098>
30. Bajaj D, Siddiquee AN, Zaman Khan N, Mukhopadhyay AK, Khan Mohammed SM, Chen D, Gangil N (2021) Flow, process forces and strains during friction stir welding: a comprehensive first principle approach. *Proc Inst Mech Eng B J Eng Manuf* 235(5):912–924. <https://doi.org/10.1177/0954405420970087>
31. Zhang J, Chen X, Xia D, Huang G, Tang A, Jiang B, Pan F (2020) Improving performance of friction stir welded AZ31/AM60 dissimilar joint by adjusting texture distribution and microstructure. *Mater Sci Eng, A* 778:139088. <https://doi.org/10.1016/j.msea.2020.139088>
32. Bao L, Le Q, Zhang Z, Cui J, Li Q (2013) Effect of homogenization treatment on microstructure evolution and the distributions of RE and Zr elements in various Mg–Li–RE–Zr alloys. *J Magnes* 1:139–144. <https://doi.org/10.1016/j.jma.2013.07.003>
33. Vaidya M, Guruvaidyathri K, Murty BS (2019) Phase formation and thermal stability of CoCrFeNi and CoCrFeMnNi equiatomic high entropy alloys. *J Alloy Compd* 774:856–864. <https://doi.org/10.1016/j.jallcom.2018.09.342>
34. Maqbool A, Lone NF, Ahmad T, Khan NZ, Siddiquee AN (2023) Effect of hybrid reinforcement and number of passes on microstructure, mechanical and corrosion behavior of WE43 Mg alloy based metal matrix composite. *J Manuf Process* 89:170–181. <https://doi.org/10.1016/j.jmapro.2023.01.070>
35. Hadorn JP, Hantzsche K, Yi S, Bohlen J, Letzig D, Agnew SR (2012) Effects of solute and second-phase particles on the texture of Nd-containing Mg alloys. *Metall and Mater Trans A* 43(4):1363–1375. <https://doi.org/10.1007/s11661-011-1018-z>
36. Wen B, Wang F, Jin L, Dong J (2016) Fatigue damage development in extruded Mg–3Al–Zn magnesium alloy. *Mater Sci Eng, A* 14(667):171–178. <https://doi.org/10.1016/j.msea.2016.05.009>
37. Zhou MR, Sun YF, Morisada Y, Shi QY, Fujii H (2023) The material flow and texture-weakening mechanism in double-sided friction stir welded Mg alloy. *Sci Technol Weld Joining* 28(2):154–161. <https://doi.org/10.1080/13621718.2022.2139451>
38. Park SH, You BS (2015) Effect of homogenization temperature on the microstructure and mechanical properties of extruded Mg–7Sn–1Al–1Zn alloy. *J Alloy Compd* 637:332–338. <https://doi.org/10.1016/j.jallcom.2015.03.030>
39. PR Rios GS Fonseca da 2010 Grain boundary pinning by particles In *Materials Science Forum* 638 3907 3912 *Trans Tech Publications Ltd* <https://doi.org/10.4028/www.scientific.net/MSF.638-642.3907>
40. Sirong YU, Xianjun C, HUANG Z, Yaohui L, (2010) Microstructure and mechanical properties of friction stir welding of AZ31B magnesium alloy added with cerium. *J Rare Earths* 28(2):316–320. [https://doi.org/10.1016/S1002-0721\(09\)60104-6](https://doi.org/10.1016/S1002-0721(09)60104-6)
41. Afrin N, Chen DL, Cao X, Jahazi M (2008) Microstructure and tensile properties of friction stir welded AZ31B magnesium alloy. *Mater Sci Eng, A* 472(1–2):179–186. <https://doi.org/10.1016/j.msea.2007.03.018>
42. Liu F, Liu J, Ji Y, Bai Y (2021) Microstructure, mechanical properties, and corrosion resistance of friction stir welded Mg–Al–Zn alloy thick plate joints. *Weld World* 65:229–241. <https://doi.org/10.1007/s40194-020-01012-z>
43. Khalid E, Shunmugasamy VC, Mansoor B (2022) Microstructure and tensile behavior of a Bobbin friction stir welded magnesium alloy. *Mater Sci Eng A* 18(840):142861. <https://doi.org/10.1016/j.msea.2022.142861>
44. Zhang J, Zhang Y, Chen X, Li Z, Huang G, Pan F (2023) Improving joint performance of friction stir welded AZ31/AM60 dissimilar Mg alloys by double-sided welding. *Mater Sci Eng A* 24(882):145444. <https://doi.org/10.1016/j.msea.2023.145444>
45. Yang J, Xiao BL, Wang D, Ma ZY (2010) Effects of heat input on tensile properties and fracture behavior of friction stir welded Mg–3Al–1Zn alloy. *Mater Sci Eng A* 527(3):708–714. <https://doi.org/10.1016/j.msea.2009.09.044>
46. Pan F, Xu A, Deng D, Ye J, Jiang X, Tang A, Ran Y (2016) Effects of friction stir welding on microstructure and mechanical properties of magnesium alloy Mg–5Al–3Sn. *Mater Des* 110:266–274. <https://doi.org/10.1016/j.matdes.2016.07.146>
47. Yang J, Wang D, Xiao BL, Ni DR, Ma ZY (2013) Effects of rotation rates on microstructure, mechanical properties, and fracture behavior of friction stir-welded (FSW) AZ31 magnesium alloy. *Metall and Mater Trans A* 44:517–530. <https://doi.org/10.1007/s11661-012-1373-4>
48. Commin L, Dumont M, Masse JE, Barrallier L (2012) Friction stir welding of AZ31 magnesium alloy rolled sheets: influence of processing parameters. *Acta Mater* 57(2):326–334. <https://doi.org/10.1016/j.actamat.2008.09.011>
49. Makar GL, Kruger JL (1993) Corrosion of magnesium. *Int Mater Rev* 38(3):138–153. <https://doi.org/10.1179/imr.1993.38.3.138>
50. Hu H, Nie X, Ma Y (2014) Corrosion and surface treatment of magnesium alloys. In: Frank Czerwinski (ed) *Magnesium alloys-properties in solid and liquid states*, IntechOpen, Croatia 2014 67–108
51. Howlett PC, Gramet S, Lin J, Efthimiadis J, Chen XB, Birbilis N, Forsyth M (2012) Conversion coatings of Mg-alloy AZ91D using trihexyl (tetradecyl) phosphonium bis (trifluoromethanesulfonyl) amide ionic liquid. *Sci China Chem* 55:1598–1607. <https://doi.org/10.1007/s11426-012-4677-8>
52. Du J, Yang J, Kuwabara M, Li W, Peng J (2009) Effect of strontium on the grain refining efficiency of Mg–3Al alloy refined by carbon inoculation. *J Alloy Compd* 470(1–2):228–232. <https://doi.org/10.1016/j.jallcom.2008.03.012>
53. Gusieva K, Davies CHJ, Scully JR, Birbilis N (2015) Corrosion of magnesium alloys: the role of alloying. *Int Mater Rev* 60(3):169–194. <https://doi.org/10.1179/1743280414Y.0000000046>
54. Esmaily M, Svensson JE, Fajardo S, Birbilis N, Frankel GS, Virtanen S, Arrabal R, Thomas S, Johansson LG (2017) Fundamentals and advances in magnesium alloy corrosion. *Prog Mater Sci* 89:92–193. <https://doi.org/10.1016/j.pmatsci.2017.04.011>

55. Ghorbanpour S, McWilliams BA, Knezevic M (2019) Effect of hot working and aging heat treatments on monotonic, cyclic, and fatigue behavior of WE43 magnesium alloy. *Mater Sci Eng A* 747:27–41. <https://doi.org/10.1016/j.msea.2019.01.056>
56. Zheng T, Hu Y, Yang S (2017) Effect of grain size on the electrochemical behavior of pure magnesium anode. *J Magnes Alloy* 5(4):404–411. <https://doi.org/10.1016/j.jma.2017.09.003>
57. Argade GR, Panigrahi SK, Mishra RS (2012) Effects of grain size on the corrosion resistance of wrought magnesium alloys containing neodymium. *Corros Sci* 58:145–151. <https://doi.org/10.1016/j.corsci.2012.01.021>

**Publisher's Note** Springer Nature remains neutral with regard to jurisdictional claims in published maps and institutional affiliations.

Springer Nature or its licensor (e.g. a society or other partner) holds exclusive rights to this article under a publishing agreement with the author(s) or other rightsholder(s); author self-archiving of the accepted manuscript version of this article is solely governed by the terms of such publishing agreement and applicable law.